

Article

pH-Responsive Drug Delivery and Imaging Study of Hybrid Mesoporous Silica Nanoparticles

Zhongtao Li ¹, Jing Guo ², Guiqiang Qi ¹, Meng Zhang ³ and Liguao Hao ^{1,*} 

¹ Department of Molecular Imaging, School of Medical Technology, Qiqihar Medical University, Qiqihar 161006, China

² Department of Molecular Imaging, The First Affiliated Hospital of Qiqihar Medical University, Qiqihar 161041, China

³ Laboratory Animal Center, Qiqihar Medical University, Qiqihar 161006, China

* Correspondence: haoliguao@qmu.edu.cn

Abstract: A system of pH-responsive and imaging nanocarriers was developed using mesoporous silica nanoparticles (MSNs), in which gadolinium (Gd) was doped through in situ doping (Gd₂O₃@MSN). Sodium alginate (SA) was attached to the surfaces of the amino groups of MSNs (NH₂-Gd₂O₃@MSN) through the electrostatic adsorption between the amino groups and the carboxyl groups with the formation of hybrid SA-Gd₂O₃@MSN nanoparticles (NPs). The SA-coated NPs were spherical or near-spherical in shape with an average size of nearly 83.2 ± 8.7 nm. The in vitro drug release experiments of a model rhodamine B (RhB) cargo were performed at different pH values. The result confirmed the pH-responsiveness of the nanocarriers. The results of the cytotoxicity studies indicated that the SA-Gd₂O₃@MSN NPs were not cytotoxic by themselves. The results of the in vivo safety evaluation and the hemolysis assay confirmed that the system is highly biocompatible. It is noteworthy that the T1 contrast of the system was significantly enhanced by the Gd, as indicated by the result of the MR imaging. This study confirms that the synthesized hybrid nanosystem is promising for pH-responsive drug delivery and MR imaging for cancer diagnosis and treatment.

Keywords: mesoporous silica; pH-responsive; magnetic resonance imaging; drug delivery; controlled release



Citation: Li, Z.; Guo, J.; Qi, G.; Zhang, M.; Hao, L. pH-Responsive Drug Delivery and Imaging Study of Hybrid Mesoporous Silica Nanoparticles. *Molecules* **2022**, *27*, 6519. <https://doi.org/10.3390/molecules27196519>

Academic Editor: Ali Nazemi

Received: 30 August 2022

Accepted: 28 September 2022

Published: 2 October 2022

Publisher's Note: MDPI stays neutral with regard to jurisdictional claims in published maps and institutional affiliations.



Copyright: © 2022 by the authors. Licensee MDPI, Basel, Switzerland. This article is an open access article distributed under the terms and conditions of the Creative Commons Attribution (CC BY) license (<https://creativecommons.org/licenses/by/4.0/>).

1. Introduction

Nanotechnology has supplied a novel arsenal to drug delivery systems over the past few years, which has inspired a novel field, i.e., nano-drug delivery systems (NDDSs). The benefits of using an NDDS versus conventional chemotherapy involve the increased bioavailability, solubility of the drugs, and pharmacokinetics behavior in vivo, thereby reducing the side effects and increasing the curative effect of the therapies [1]. The common NDDSs include polymers, dendrimers, inorganic nanoparticles and organic-inorganic hybrid nanosystems [2–6]. Among the above nanosystems, mesoporous silica nanoparticles (MSNs) have attracted the attention of numerous researchers and have become the highly popular drug nanocarriers for their facile production, tunable uniform pore size, large pore volume, high surface area, and great drug loading capacity [7,8]. A dedicated mesoporous silica NDDS design has been extensively used [9,10] since silica-based materials have been considered safe by the United States Food and Drug Administration.

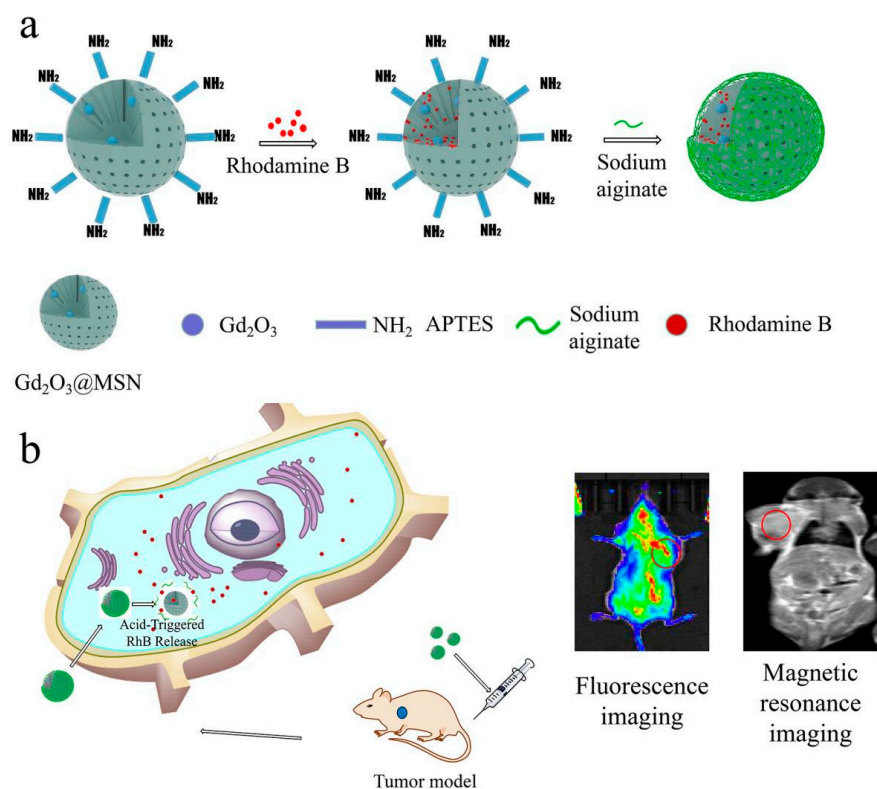
Additionally, research on innovative multifunctional nanosystems with the combination of imaging and therapy has become a hotspot. Magnetic resonance imaging (MRI), nuclear medicine imaging (NMI), and ultrasound (US) techniques have been extensively used [11–14] in the context of medical imaging modalities (e.g., computed tomography (CT)). To be specific, MRI is a popular imaging technology due to its high-resolution morphological capabilities, non-invasiveness, and lack of risk of radiation damage [15,16]. More excitingly, incorporating the MRI contrast agents (e.g., gadolinium oxide (Gd₂O₃))

into nanosystems can extend the blood circulation time while endowing the nanosystems with MRI visibility by taking the shortened longitudinal proton relaxation time of the surrounding hydrogen protons [17,18].

To achieve the release of the drug in the targeted diseased tissues, several surface-functionalized coatings as gatekeepers are modified onto the MSN carriers to block the drug in the pore channels [19–22]. Various types of stimuli could be used to open the gatekeepers, such as pH [23,24], enzymes [25], redox [26,27], light [28], ultrasound [29], and temperature [30]. Among them, pH-responsive systems have gained wide attention because of the distinct pH values in different tissues (e.g., healthy or tumor tissues) [31]. For this reason, a pH-dependent NDDS has been designed for pH-triggered drug release.

Sodium alginate (SA), an anion- and water-soluble linear polysaccharide, comprises 1-4-linked β -D-mannuronate (M) and α -L-guluronate (G) [32]. SA has been widely employed in pharmaceutical excipients for its fascinating advantages (including its safety, biocompatibility, and biodegradability [33–36]). SA is relatively low-cost and easily available via the isolation from cell walls of brown algae (*Ascophyllum nodosum* and *Laminaria digitata*) as compared with polymers and polyelectrolytes [33,37]. Moreover, the existing research has reported that SA is capable of making nanoparticles more dispersible and stable [38]. Accordingly, the polysaccharide SA was selected as a capping agent for its high biodegradability and appropriate size to cover the MSNs so as to control the drug release.

A pH-responsive delivery and imaging nanosystem was developed in this study (Scheme 1). In the developed system, the MSNs ($Gd_2O_3@MSN$) were prepared by doping Gd^{3+} . The polysaccharide SA was attached onto the surfaces of the MSNs through electrostatic adsorption, which served as the pH-sensitive end-cap, while providing better biocompatibility. RhB was adopted as the model drug to study the loading capacity of the MSNs. Moreover, in vitro drug release experiments were performed to examine the pH-responsive release under acidic conditions [39,40]. Furthermore, the Gd^{3+} -incorporated MSNs can serve as MRI contrast agents to monitor drug delivery.



Scheme 1. Schematic diagram of the preparation of SA- $Gd_2O_3@MSN$ nanocomposites (a) and their application in MR imaging and pH-triggered release in the tumor cells (b).

2. Results and Discussion

2.1. Synthesis and Characterization

Nanotheranostic platforms are capable of efficiently integrating the processes of diagnosis and therapeutic moiety. A hybrid nanocarrier was successfully synthesized for MR imaging and drug loading in this study. Scheme 1a illustrates the synthesis of RhB-loaded SA-Gd₂O₃@MSN hybrid systems. First, Gd³⁺-doped MSN nanoparticles (Gd₂O₃@MSN) were prepared. Subsequently, the surfaces of Gd₂O₃@MSN were grafted with APTES to become amino-functionalized Gd₂O₃@MSN (NH₂-Gd₂O₃@MSN). Next, SA was modified onto the NH₂-Gd₂O₃@MSN surfaces through the electrostatic interaction between the amino group of NH₂-Gd₂O₃@MSN and the carboxyl group in SA [38,41,42]. As depicted in the high-resolution TEM image in Figure 1a, the average diameter of the Gd₂O₃@MSN reached 77.5 ± 9.4 nm, and the Gd₂O₃@MSN exhibited a clearly defined pore structure and regular morphology. Compared with the smooth surface of Gd₂O₃@MSN, the grafted polysaccharide SA-Gd₂O₃@MSN surface (Figure 1b) was blurred, indicating that the SA covered the MSN carrier. EDS mapping images (Figure 1d) showed the coexistence of Gd, Si, and O in the Gd₂O₃@MSN NPs. Afterward, the elemental content was further analyzed using the EDS spectrum (Figure 1c), and the exact content of gadolinium was identified as 5.3 wt% through an ICP-MS (Agilent 720 ES, Shanghai, China) analysis. The above results significantly indicated that the Gd element was successfully loaded into the MSNs.

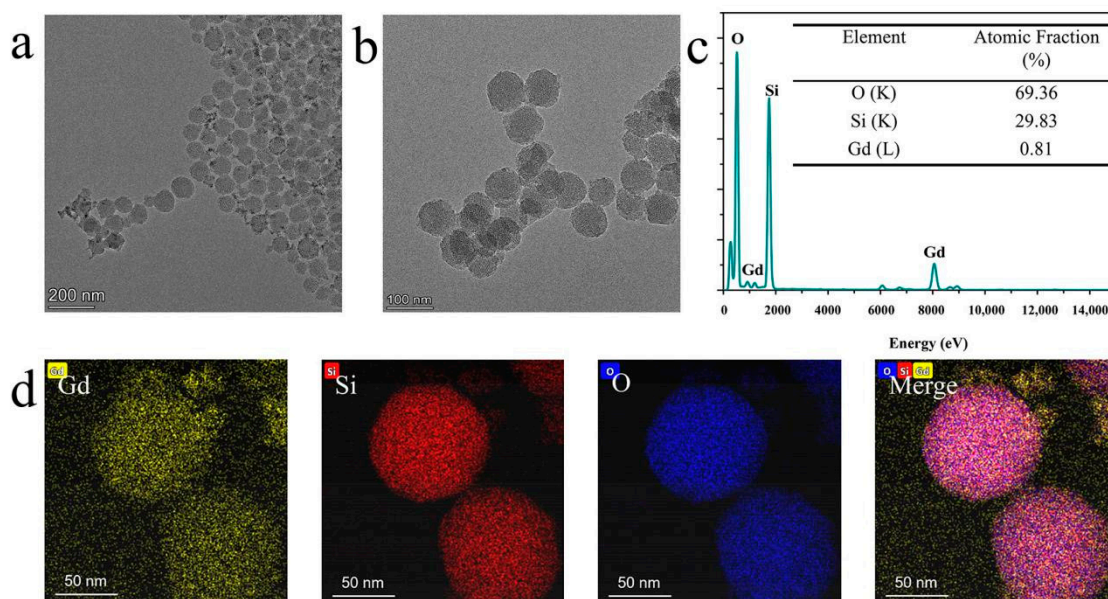


Figure 1. TEM images of (a) Gd₂O₃@MSN and (b) SA-Gd₂O₃@MSN. (c) EDS spectrum of Gd₂O₃@MSN NPs; inset: table showing the quantification of the respective element. (d) EDS elemental mapping of Gd₂O₃@MSN.

The successful synthesis of all products was achieved using a variety of methods. The zeta potential of NH₂-Gd₂O₃@MSN underwent a great change after functionalization, varying from −21.9 to +28.7 mV (Figure 2a), which indicated the addition of the amine groups to the surface of Gd₂O₃@MSN. Upon the encapsulation of SA, the surface charge of the SA-Gd₂O₃@MSN was significantly decreased to −21.1 mV, which could be explained by the considerable carboxyl groups in the SA polysaccharide [43]. The hydrodynamic diameter and PDI values of Gd₂O₃@MSN, NH₂-Gd₂O₃@MSN, and SA-Gd₂O₃@MSN were obtained in ddH₂O (Figure 2b,c). The diameters of Gd₂O₃@MSN and NH₂-Gd₂O₃@MSN were 168.7 nm and 193.6 nm, respectively. The hydrodynamic diameter increased to 233.4 nm after the addition of SA on the surfaces of NH₂-Gd₂O₃@MSN to form SA-Gd₂O₃@MSN. The PDI of SA-Gd₂O₃@MSN was smaller than that of NH₂-Gd₂O₃@MSN. In addition, the diameters obtained via TEM were smaller than those examined via DLS, probably due to the

slight aggregation and hydration layer of NPs under aqueous conditions [44,45]. Figure 2d presents the FT-IR spectra of $\text{Gd}_2\text{O}_3@\text{MSN}$, $\text{NH}_2\text{-Gd}_2\text{O}_3@\text{MSN}$, $\text{SA-Gd}_2\text{O}_3@\text{MSN}$, and SA. The produced peaks were at 1080 cm^{-1} , corresponding to Si-O-Si vibration. Next, the presence of amine groups (NH_2 -) on the $\text{NH}_2\text{-Gd}_2\text{O}_3@\text{MSN}$ surfaces was indicated by the appearance of the characteristic peak (N-H) at 2900 cm^{-1} [46]. After SA was added to the $\text{NH}_2\text{-Gd}_2\text{O}_3@\text{MSN}$ surface, there was an increase in the adsorption peaks at 1400 cm^{-1} , due to the vibration of $-\text{COOH}$ in the SA [29]. All of the results confirm the successful preparation of $\text{SA-Gd}_2\text{O}_3@\text{MSN}$.

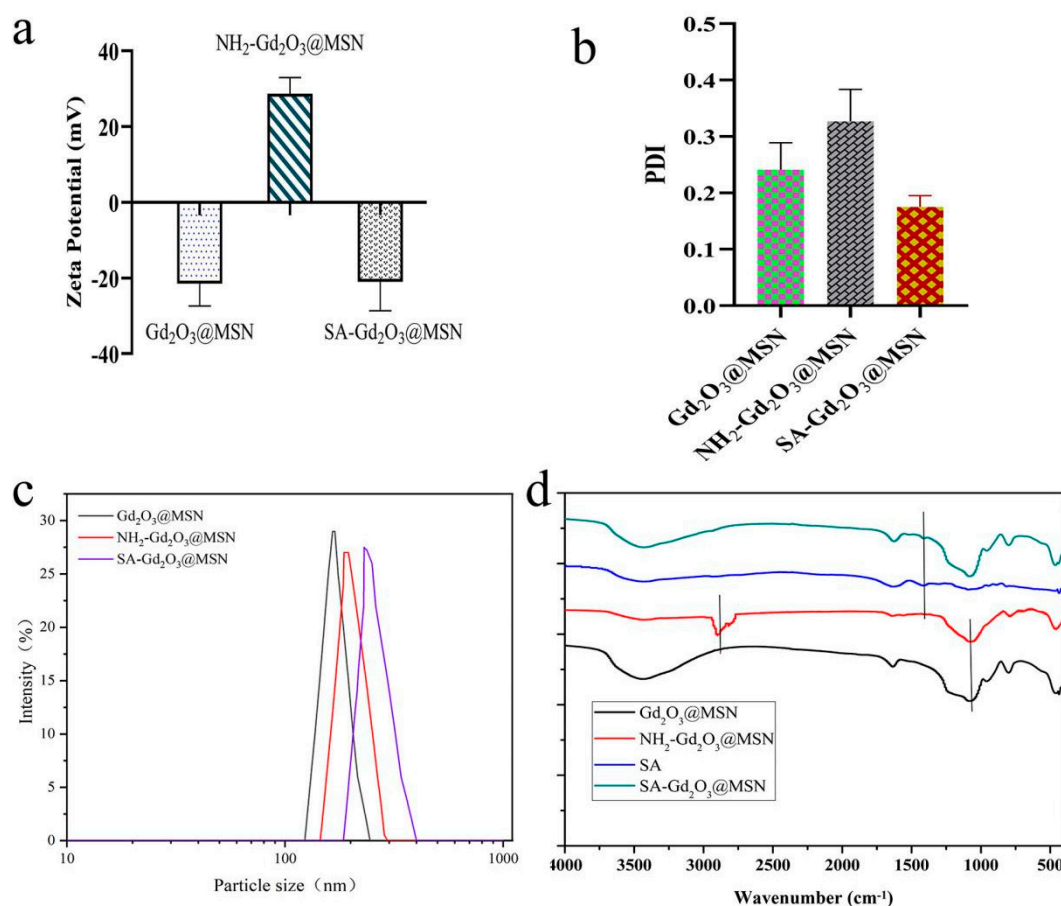


Figure 2. Structural characterization: (a) zeta potentials, (b) PDI values, and (c) hydrodynamic diameters of $\text{Gd}_2\text{O}_3@\text{MSN}$, $\text{NH}_2\text{-Gd}_2\text{O}_3@\text{MSN}$, and $\text{SA-Gd}_2\text{O}_3@\text{MSN}$; (d) FT-IR spectra of $\text{Gd}_2\text{O}_3@\text{MSN}$, $\text{NH}_2\text{-Gd}_2\text{O}_3@\text{MSN}$, $\text{SA-Gd}_2\text{O}_3@\text{MSN}$, and SA.

In addition, the pore size distributions and surface areas of a range of modified MSN nanoparticles were examined through the N_2 adsorption–desorption measurements at 77 K (Figure 3 and Table 1). In brief, the curve of NPs was analyzed using the Brunauer–Emmett–Teller method. The surface area and pore volume of $\text{Gd}_2\text{O}_3@\text{MSN}$ were $956.18\text{ m}^2/\text{g}$ and $0.74\text{ cm}^3/\text{g}$, respectively. For $\text{SA-Gd}_2\text{O}_3@\text{MSN}$, the above parameters were reduced to $672.09\text{ m}^2/\text{g}$ and $0.45\text{ cm}^3/\text{g}$, respectively, indicating that SA coated the MSN surfaces.

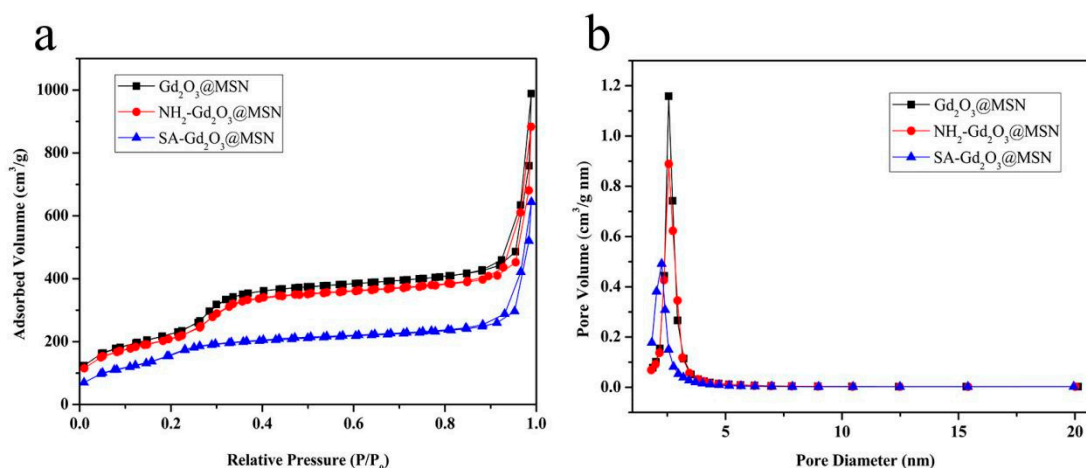


Figure 3. (a) The nitrogen adsorption–desorption isotherms and (b) pore size distributions of Gd₂O₃@MSN, NH₂-Gd₂O₃@MSN, and SA-Gd₂O₃@MSN.

Table 1. The N₂ adsorption and desorption parameters of different functionalized MSN nanoparticles.

	Surface Area (m ² /g)	Pore Volume (cm ³ /g)	Pore Size (nm)
Gd ₂ O ₃ @MSN	956.18	0.74	3.17
NH ₂ -Gd ₂ O ₃ @MSN	888.07	0.69	3.15
SA-Gd ₂ O ₃ @MSN	672.09	0.45	2.96

2.2. Release Experiments from SA-Coated Mesoporous Silica

A series of release experiments were performed to examine the pH-responsiveness of the hybrid mesoporous silica, using a model fluorescent RhB as the cargo. The successful RhB loading on the nanocarrier was evidenced by the FT-IR spectra of the samples (Figure S3). The LC of SA-Gd₂O₃@MSN-RhB was 18.9 µg/mg. To simulate the physiological conditions, the RhB-loaded and SA-coated NPs were incubated at 37 °C, using three pH values (7.4, 5.5, and 4.5), corresponding to the normal blood, endosome, and lysosomal environments, respectively (Figure 4a) [47,48]. At neutral pH (7.4), 18.2% of the RhB was released after 48 h of incubation. However, the RhB release contents were increased to 52.1% at pH 5.5 and to 81.2% at pH 4.5, respectively. These results were attributed to the weakened electrostatic interaction between the negatively charged carboxylic acid group of the SA and the positively charged MSNs, leading to the opening of the mesoporous MSNs [49–52]. The above result suggests that the release of RhB is significantly pH-dependent.

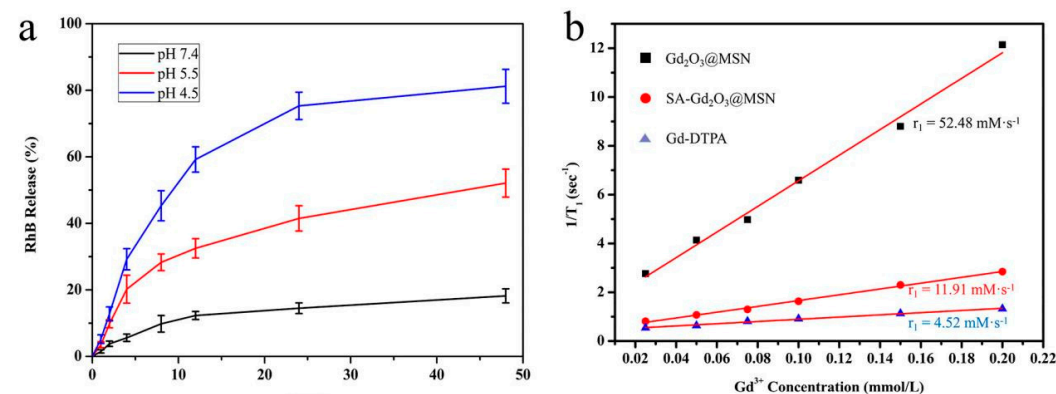


Figure 4. Physicochemical characterization: (a) RhB release profiles from the aqueous dispersions of SA-Gd₂O₃@MSN (1 mg/mL) at varying pHs, where error bars indicate the standard deviation (n = 3 per condition); (b) T₁ relaxation rate (r₁) recorded at 0.5 T as a function of the Gd³⁺ concentrations (pH 7.4) for Gd₂O₃@MSN, Gd-DTPA, and SA-coated NH₂-Gd₂O₃@MSN.

In addition, the 48 h cumulative drug release rates from MSN NPs without SA coating at pH 7.4 and pH 5.5 were higher than the cumulative drug release rate from SA-Gd₂O₃@MSN-RhB NPs at 48 h, which clearly showed that SA is capable of hampering the dye release (Figure S5).

2.3. Assessment of the T1 Relaxivity

The results of this study confirmed the pH-triggered release of RhB from hybrid mesoporous silica. Next, the potential use of SA-Gd₂O₃@MSN as an MRI contrast agent was examined using the 0.5 T NMI20 Analyst NMR system. The relaxivity (r_1) rates of Gd₂O₃@MSN and SA-Gd₂O₃@MSN were respectively obtained as 52.48 mM⁻¹s⁻¹ ($R^2 = 0.9916$) and 11.91 mM⁻¹s⁻¹ ($R^2 = 0.9911$) at 0.5 T, which were significantly higher than for the clinically applied Gd-DTPA ($r_1 = 4.52$ mM⁻¹s⁻¹, $R^2 = 0.9961$), suggesting that the Gd₂O₃@MSN may serve as an MRI contrast agent (Figure 4b). The lower relaxation of SA-Gd₂O₃@MSN compared with Gd₂O₃@MSN was tentatively attributed to the SA coating preventing the water molecules from entering the mesoporous structure, resulting in less water molecules being bound to the Gd center [53,54].

2.4. Colloidal Stability

To compare their colloidal stability levels, Gd₂O₃@MSN, NH₂-Gd₂O₃@MSN, and SA-Gd₂O₃@MSN were suspended in ddH₂O, saline, and RPMI 1640 medium supplemented with 10% FBS at 37 °C for 24 h. As depicted in Figure S6, SA-Gd₂O₃@MSN remained stable in ddH₂O, saline, and the medium for over 24 h without precipitation, while the structural integrity was maintained. In contrast, Gd₂O₃@MSN and NH₂-Gd₂O₃@MSN quickly flocculated in the respective buffers. The hydrodynamic diameter of SA-Gd₂O₃@MSN was further examined using DLS, and the results indicated that no significant size changes occurred in the respective buffers (Figure 5). Afterward, free Gd ions in the above solutions were detected using ICP-MS, indicating that SA-Gd₂O₃@MSN only released negligible amounts of free Gd³⁺ (Figure S8). The above data suggest that the SA coating can increase the stability of hybrid mesoporous silica.

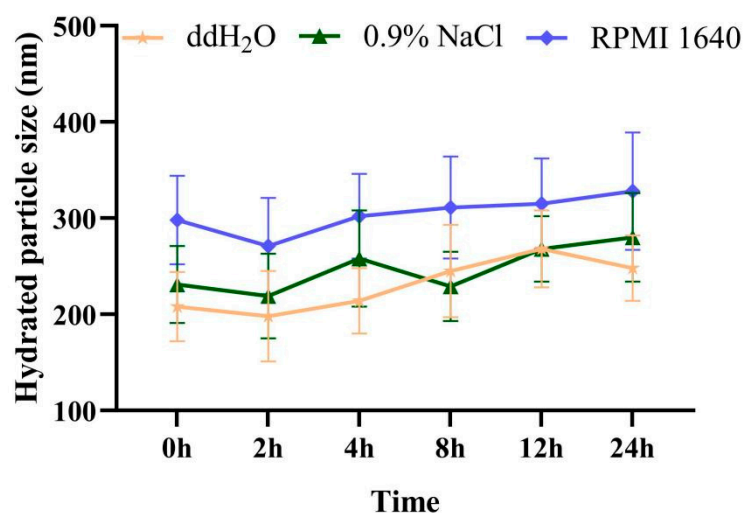


Figure 5. The size change of SA-Gd₂O₃@MSN after incubation in ddH₂O, 0.9% NaCl, and RPMI 1640 (with 10% FBS) for different periods. Error bars represent the standard deviations of the three analytical replicates.

2.5. Biocompatibility and Biototoxicity

A safe nanocarrier system is a prerequisite for further applications. Accordingly, the *in vitro* cytotoxicity was examined using a CCK-8 assay. As depicted in Figure 6a, the viability of the 4T1 cells and MCF-7 cells was over 80% even after treatment with 200 µg/mL SA-Gd₂O₃@MSN, similar to other NPs (Figure S9), suggesting that SA-coated

NPs exhibit negligible toxicity. A hemolysis assay was then performed to examine the hemocompatibility of SA-Gd₂O₃@MSN. As depicted in Figure 6c, the hemolysis rate was less than 5% for all concentrations, meeting the hemolysis criterion for biomaterials [55,56]. Furthermore, the optical images confirmed that the red blood cells remained intact even after treatment with 800 µg/mL SA-Gd₂O₃@MSN (Figure S10).

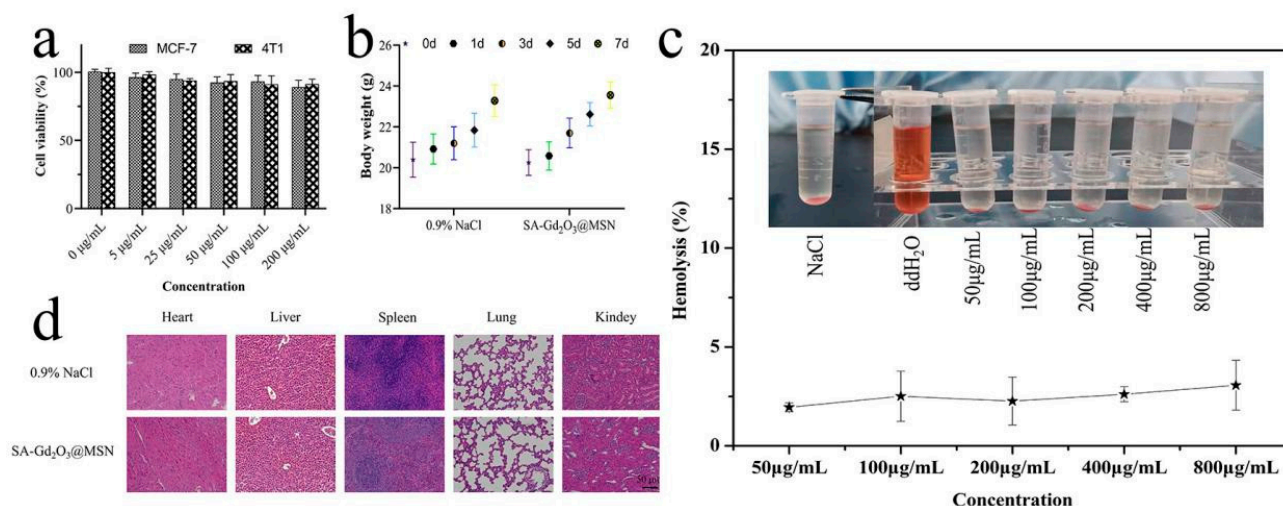


Figure 6. Biocompatibility and biotoxicity: (a) viability of 4T1 cells and MCF-7 cells upon treatment with SA-Gd₂O₃@MSN for 24 h; (b) weight changes of mice after treatment for a week, with data expressed as means ± SD (n = 5); (c) hemolytic efficiency of SA-Gd₂O₃@MSN to human red blood cells; (d) H&E staining of organs dissected from mice upon treatment with 0.9% NaCl and SA-Gd₂O₃@MSN (50 mg/kg).

The SA-Gd₂O₃@MSN solution (50 mg/kg) was intravenously injected into healthy Balb/c mice, and the above animals were monitored for 7 days to examine the in vivo biotoxicity from the SA-coated NPs. As depicted in Figure 6b, the body weights of mice in the SA-Gd₂O₃@MSN group increased slightly, which were similar to those of the saline group. Then, the results of the H&E staining assay indicated that the major organs of the SA-Gd₂O₃@MSN treated mice (e.g., heart, liver, spleen, lung, and kidney) did not exhibit any pathological changes (Figure 6d). No deaths of mice were identified during the experimental process. All of the results suggest that SA-Gd₂O₃@MSN exhibits high biocompatibility and can have in-depth applications.

2.6. Cellular Uptake of Multifunctional Nanocomposites

To examine the intracellular drug release behaviors of RhB, 4T1 cells were incubated with RhB-loaded and SA-coated NPs for different periods of time and imaged under a CLSM (Figure 7a). As depicted in the CLSM images, the RhB fluorescence (red color) accumulated in the nucleus and cytoplasm of the cells, which was probably due to the pH-induced RhB release from the nanocarriers. Notably, the RhB fluorescence within the cells increased as the incubation time was extended (Figure S11a,b). To further examine the intracellular MRI performance and cellular uptake efficiency, the NPs-treated (100 µg/mL) 4T1 cells were collected and fixed in centrifuge tubes and then examined using a clinical 3.0T MRI scanner (Figure 7b). As depicted in Figure S11c, the 4T1 cells after treatment for 24 h exhibited the highest MR signal intensity. The above results suggest that more NPs are successfully taken up by the cells over time.

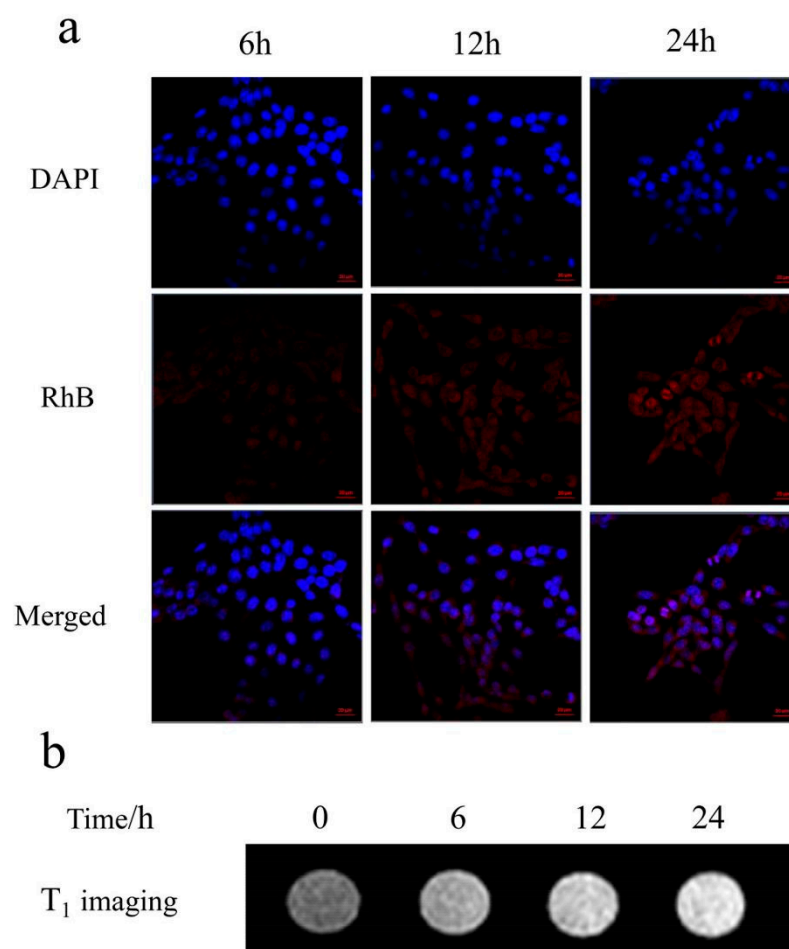


Figure 7. Cellular internalization of SA-Gd₂O₃@MSN-RhB NPs: (a) CLSM images of 4T1 cells incubated with SA-Gd₂O₃@MSN-RhB nanoparticles at different time points, where red and blue represent RhB and DAPI fluorescence, respectively (scale bar: 20 μm); (b) T₁-weighted MR images of a tube containing SA-Gd₂O₃@MSN-RhB NP-labeled 4T1 cells.

2.7. In Vivo Proof-of-Concept Study: Preliminary In Vivo Short-Term pH Triggering and MR Imaging Performance

To further examine the in vivo pH-triggering of the carrier designed here, the experiments were performed in 4T1 tumor-bearing mice. Fluorescent RhB was selected as the model drug and the release from the carrier was monitored via near-infrared fluorescence imaging (Figure 8a). At 48 h post-injection, a significant fluorescence signal was identified at the tumor site in the SA-Gd₂O₃@MSN-RhB group. In addition, the fluorescence signal at the tumor site in the SA-Gd₂O₃@MSN-RhB group was stronger than that in the NH₂-Gd₂O₃@MSN-RhB group. In contrast, the fluorescence signal was not identified at the tumor site in the RhB group. During the imaging process, the fluorescent signal in the SA-Gd₂O₃@MSN-RhB group was more persistent in the tumor site than NH₂-Gd₂O₃@MSN-RhB and RhB, since the SA-coated NPs can control the release of the drug and the successful pH-triggered dissociation caused by endogenous acids.

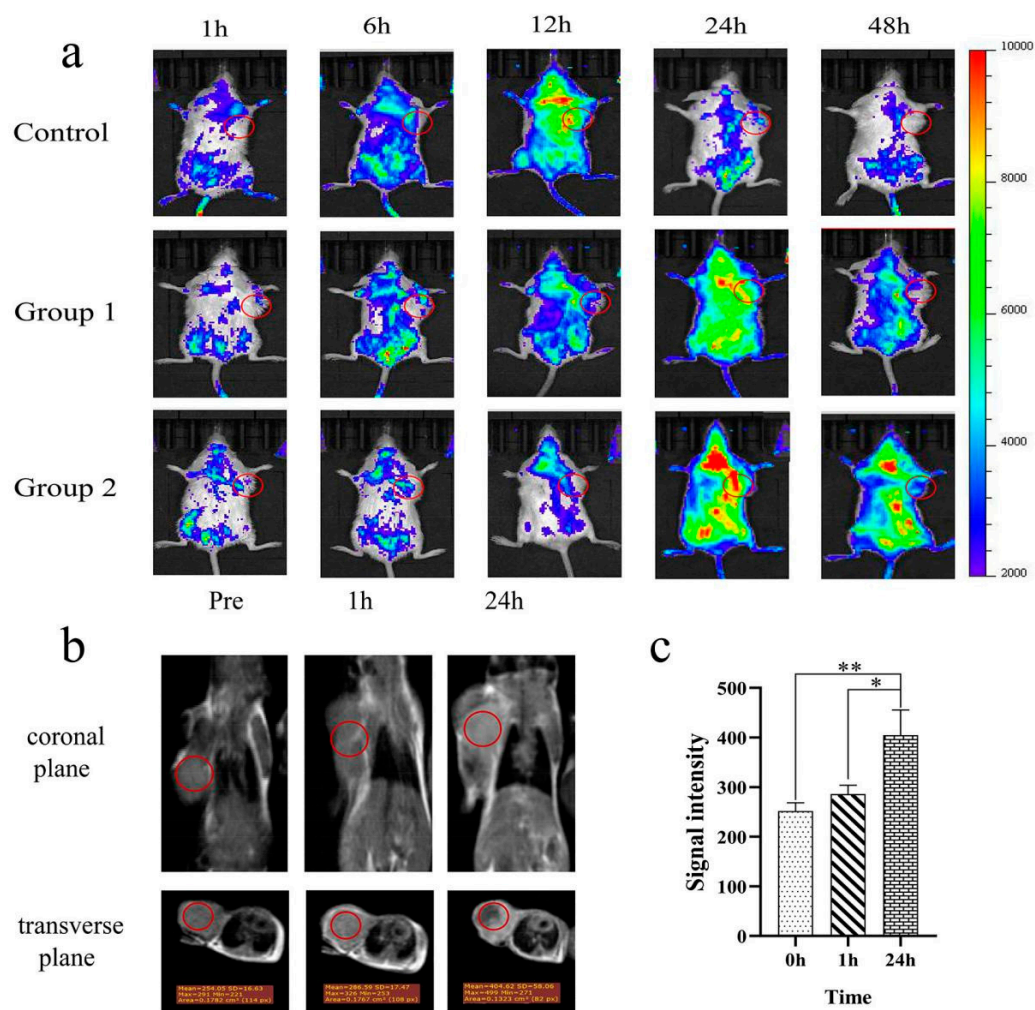


Figure 8. In vivo multimodal imaging. (a) Fluorescence images of Balb/c mice bearing 4T1 tumors at 1, 6, 12, 24, and 48 h after the injection of NPs. Control, only RhB; group 1, $\text{NH}_2\text{-Gd}_2\text{O}_3\text{@MSN-RhB}$; group 2, $\text{SA-Gd}_2\text{O}_3\text{@MSN-RhB}$. (b) Time-dependent T1-weighted MRI images and (c) signal intensity changes. Data are expressed as means \pm SD ($n = 3$) (* $p < 0.05$, ** $p < 0.01$).

For in vivo imaging applications, the T1-weighted MR imaging of the tumor-bearing mice was also performed to verify the feasibility of $\text{SA-Gd}_2\text{O}_3\text{@MSN-RhB}$ as an in vivo MRI contrast agent. The NPs were injected into 4T1 tumor-bearing mice. As depicted in Figure 8b,c, the signal intensity at the tumor site was significantly enhanced. The above results suggested that the as-prepared NPs could be used as potential contrast agents for the MR imaging of tumors.

3. Materials and Methods

3.1. Materials

The cetyltrimethylammonium bromide (CTAB) was provided by Coolaber Science and Technology (Beijing, China). The tetraethylorthosilicate (TEOS) was purchased from Fuchen Chemical Reagents (Tianjin, China). The 3-aminopropyl-triethoxysilane (APTES) and rhodamine B (RhB) were offered by Macklin Biochemical Co., Ltd. (Shanghai, China). The sodium aiginate (SA) and gadolinium(III) chloride hexahydrate ($\text{GdCl}_3 \cdot 6\text{H}_2\text{O}$) originated from Aladdin Biochemical Technology Co., Ltd. (Shanghai, China). The RPMI 1640 cell culture medium and fetal bovine serum (FBS) were purchased from Gibco (Thermo Fisher Scientific, Waltham, MA, USA). All chemicals used for synthesis were used directly without further purification unless otherwise specified.

3.2. Synthesis of SA-Gd₂O₃@MSN

3.2.1. Synthesis NH₂-Gd₂O₃@MSN

The MSNs (Gd₂O₃@MSN) were prepared in accordance with our previous research [57]. In brief, a mixture of NaOH (140 mg) and CTAB (500 mg) in ddH₂O (220 mL) was stirred at 80 °C for 1 h. Subsequently, the TEOS (1.5 mL) was added dropwise to the above mixture through appropriate stirring (250 rpm). The GdCl₃·6H₂O aqueous solution (20 mL, 5 mg/mL) was rapidly introduced into the mixture after reacting for 2 h at 80 °C. An additional 1 mL of TEOS was added to the above samples 1 h later. Subsequently, the nanoparticles (NPs) were centrifuged after being stirred for 1 h to collect the samples. Next, the collected samples were dried under vacuum. The resulting NPs were calcined at 600 °C for 4 h to remove the CTAB surfactants (Figure S1). Here, 2 mL of APTES and 500 mg of Gd₂O₃@MSN were added to 30 mL of ethanol to obtain an amino-functionalized MSN solution (NH₂-Gd₂O₃@MSN), and the solution was then stirred at 30 °C for 36 h [58]. The synthesized NH₂-Gd₂O₃@MSN was collected through centrifugation, washed three times with ethanol, and dried under vacuum for further use.

3.2.2. Synthesis SA-Gd₂O₃@MSN

Here, 200 mg of SA was added to 10 mL double-distilled water (ddH₂O) to prepare the SA solution. Subsequently, 100 mg of NH₂-Gd₂O₃@MSN was dispersed in 30 mL of ddH₂O. Next, the SA solution (6 mL) was poured into the suspension and then stirred for 24 h at ambient temperature to form the SA-Gd₂O₃@MSN nanocomposites through electrostatic absorption. Lastly, the prepared NPs were centrifuged and washed to collect the samples.

3.3. Characterization

The morphological features and mesoporous network structure of the as-synthesized NPs were examined using FESEM (field emission scanning electron microscope) images (FEI Talos F200S). The elemental compositions of the samples were determined using elemental mapping and EDS (energy-dispersive spectroscopy) analyses. The BET (Brunauer–Emmett–Teller) surface area, total pore volume, and pore diameter were obtained using nitrogen sorption isotherms (Micromeritics ASAP-2460, Norcross, GA, United States). The FT-IR spectra were examined using a FT-IR spectrometer (FT-IR 6800 JASCO, Marseille, France) in the 400–4000 cm⁻¹ region using the KBr pellet technique. The zeta potential and size were recorded with a Nano-z90 Nanosizer (Malvern Instruments Ltd., Worcestershire, UK) at ambient temperature.

3.4. Release Experiments with RhB-Loaded, Polysaccharide-Coated MSN Nanoparticles

The MSNs were loaded with rhodamine B (RhB) dye before the SA coating to examine the pH-responsiveness of the hybrid materials. Subsequently, 100 mg of NH₂-Gd₂O₃@MSN was dispersed in 40 mL of ddH₂O with 4 mg of RhB, then the solutions was stirred for 24 h at ambient temperature. Afterward, the above protocol for the grafting of the polymers was followed again. The loading capacity (LC) of the RhB was calculated according to the following equation:

$$LC = \frac{m_A - m_B}{m_A - m_B + m_C} \quad (1)$$

In which m_A was the added mass of the RhB, m_B was the mass of the RhB in the supernatant, and m_C was the total mass of the NH₂-Gd₂O₃@MSN.

The particles (SA-Gd₂O₃@MSN-RhB, 5 mg) were soaked in 5 mL PBS buffer solutions (pH 7.4, 5.5, and 4.5) at ambient temperature to examine the pH-dependent releasing efficiency. The mixed solutions were transferred into a dialysis bag ($n = 3$ for each condition). Subsequently, the samples were maintained in buffer solution and shaken at 37 °C. At timed intervals, 3 mL of solution was withdrawn, and an equal volume of fresh buffer was added after the respective sampling. The amount of released RhB was investigated using an FL (fluorospectrophotometer).

3.5. In Vitro T1 Relaxivity Evaluation

The T1 relaxivity values of SA-Gd₂O₃@MSN at varying concentrations (0.025, 0.05, 0.075, 0.100, 0.150, and 0.200 mM) of Gd were examined using a 0.5 T NMI20 Analyst NMR system (Niumag, Suzhou, China). The instrumental parameters were set as follows: sampling bandwidth (SW): 100 kHz; time wait (TW): 4000 ms; regulated first data (RFD): 0.08 ms; number of samples (NS): 8; echo time (TE): 2 ms.

3.6. Colloidal Stability

The particles were dispersed in ddH₂O, saline, or RPMI 1640 medium with 10% FBS (fetal bovine serum) at a concentration of 2 mg of NPs/mL for the colloidal stability test. The samples were mixed via ultrasonic concussion and left for 1 min. Subsequently, the change in the particle size was recorded through DLS measurements for up to 24 h.

3.7. Biocompatibility

The blood compatibility was examined through hemolysis assay experiments in accordance with previous reports [59,60]. First, fresh whole blood was taken from each volunteer, then the red blood cells (RBCs) were centrifugally isolated at 2500 rpm for 6 min at 4 °C. Subsequently, the RBCs were purified by washing them another five times with saline. Next, 2 mL of diluted RBC (4% v/v) suspension was mixed with 2 mL of SA-Gd₂O₃@MSN NPs (50, 100, 200, 400, and 800 µg/mL) dispersed in saline. The RBCs were incubated with ddH₂O and saline as a negative control and positive control, respectively. Next, the system was incubated at 37 °C for 4 h and then centrifugated at 8000 rpm for 10 min. The absorbance of the supernatants at 576 nm was examined using a UV-2450 spectrophotometer (Shimadzu, Tokyo, Japan). The hemolysis percentage was obtained as follows (repeated three times for each respective sample):

$$\text{Hemolysis}(\%) = \frac{(A_{\text{Sample}} - A_{\text{Negative Control}})}{(A_{\text{Positive Control}} - A_{\text{Negative Control}})} \times 100\% \quad (2)$$

where A_{Sample} represents the absorption intensity of the SA-Gd₂O₃@MSN-treated group; $A_{\text{Negative Control}}$ and $A_{\text{Positive Control}}$ denote the absorbance of the normal saline and ddH₂O groups, respectively.

The MCF-7 cells (HTB-22) and 4T1 cells (CRL-2539) were employed in combination with a CCK-8 assay to examine the NPs' cytotoxicity. In brief, the cells were separately plated in a 96-well plate at a density of 6×10^3 cells per well and then cultured in RPMI-1640 containing 10% FBS and 1% penicillin streptomycin at 37 °C under 5% CO₂ conditions for 24 h. Next, the SA-Gd₂O₃@MSN NPs were added to the medium at different concentrations (0, 5, 25, 50, 100, and 200 µg/mL). After being incubated for 24 h, the original medium was removed and replaced with 100 µL of fresh medium. Subsequently, CCK-8 solution (10 µL) was added to the respective well, and the cells were further incubated for 2 h. Lastly, the absorbance at 490 nm of the respective well was examined using a plate reader (SAFIRE2, TECAN, Männedorf, Switzerland).

Female Balb/c mice (18–20 g) were used as the animal models to examine the biotoxicity of the SA-Gd₂O₃@MSN NPs in vivo. All experiments gained approval from the Animal Ethics Committee of Qiqihar Medical University (No. QMU-AECC-2021-100). Saline and SA-Gd₂O₃@MSN NPs at a high dosage (50 mg/kg) were injected through the tail vein to the mice. After 7 days, all the mice were dissected, and the main organs (including the heart, liver, spleen, lungs, and kidneys) were collected and examined through histopathological examination (Leica-DM4B digital microscope, Hesse Germany).

3.8. Cellular Uptake

The cellular uptake and in vitro MR imaging capacities of the SA-Gd₂O₃@MSN-RhB NPs were examined using 4T1 cells. In brief, the 4T1 cells were incubated with 100 µg/mL

of SA-Gd₂O₃@MSN-RhB NPs for different durations (6, 12, and 24 h) after being seeded into 6-well plates (1×10^5 cells/well) and allowed to stand for overnight adhesion. Subsequently, the cells were washed thoroughly with PBS, fixed with 4% paraformaldehyde, and then stained with DAPI for CLSM (confocal laser scanning microscopy) observations. A quantitative evaluation of the cellular uptake was performed using FCM (flow cytometry). At specific points of time (6, 12, and 24 h), trypsinized cells (without EDTA) in the respective well were gently resuspended in 1 mL PBS and then analyzed with a FACS Canto flow cytometer (Becton, Dickinson, ND, USA).

To examine the MRI enhancement effect of the materials in cells, the 4T1 cells were inoculated on a 6-well culture plate incubated with 1 mL RPMI 1640 for 24 h. The cells were washed twice with PBS, then 1 mL of fresh media containing SA-Gd₂O₃@MSN-RhB NPs was introduced at a concentration of 100 µg/mL. Subsequently, the medium was removed at the preset points of time (6, 12, and 24 h). Next, the cells were digested with trypsin and then centrifuged at 1000 rpm for 6 min. Then, 0.5 mL of PBS was introduced to suspend the cells and the cells were further fixed by adding 0.5 mL of 2.0 wt% agarose solution to the centrifugation tubes. MRI scanning was performed using a Philips 3.0 T MRI scanner and a human carotid wall coil. The T1WI sequence was used as follows: TR/TE: 650 ms/10 ms; layer thickness: 3 mm; layer spacing: 2 mm; matrix: 192 × 192; FOV: 130 × 130 mm; nexus: 2 times.

3.9. In Vivo Proof-of-Concept Study

A 4T1 tumor model was built by injecting 100 µL of 4T1 cell suspension (1×10^6 cells) into the right armpit of female Balb/c mice. To examine the behavior of the RhB-loaded SA-Gd₂O₃@MSN hybrid systems in acidic pH environments, the mice were randomly assigned to three groups and treated with free RhB, RhB-loaded MSNs (NH₂-Gd₂O₃@MSN-RhB), and SA-Gd₂O₃@MSN-RhB at a dose of 200 mg/kg RhB via tail vein injection. The fluorescence images (FI) were captured at 1, 6, 12, 24, and 48 h after injection using the IVIS Lumina III imaging system (PerkinElmer, Waltham, MA, USA). The 4T1 tumor-bearing mice were injected with 100 µL of SA-Gd₂O₃@MSN NPs (1 mg of Gd³⁺ per kg) via the tail vein for in vivo MR imaging. Subsequently, the MR images were captured at 0, 1, and 24 h after injection using a 3.0T clinical MRI scanner (Philips).

3.10. Statistical Analysis

The statistical data were investigated using SPSS 20.0 software with a two-tailed Student's t-test. The error bars presented in this study represent the standard deviation (SD). Here, a *p*-value < 0.05 indicates a difference achieving statistical significance.

4. Conclusions

In this study, a imaging nanocarrier system was developed, which was functionalized with a pH-responsive polymer. The results of the colloidal stability, hemolysis assay, and toxicity experiments suggested that the SA-coated NPs can enhance the biocompatibility and stability of hybrid mesoporous silica. The in vitro and in vivo release results confirmed that SA-Gd₂O₃@MSN-RhB exhibits pH-responsive drug release behavior in acidic environments. Moreover, the developed multifunctional nanoparticles can serve as efficient probes for the MR imaging of tumor models in vivo. The results of this study suggest that the hybrid materials investigated here can be employed as smart drug delivery and imaging nanocarriers. However, our cell-based and animal-based explorations are not enough to represent medical applications, which require further studies to validate the efficacy of these NPs.

Supplementary Materials: The following supporting information can be downloaded at: <https://www.mdpi.com/article/10.3390/molecules27196519/s1>: Figure S1. Illustration of the preparation of Gd³⁺-incorporated mesoporous silica nanoparticles (MSN) (Gd₂O₃@MSN) for magnetic resonance imaging. Figure S2: Molecular structure of sodium alginate. Figure S3: FT-IR spectra of NH₂-Gd₂O₃@MSN-RhB and RhB. Figure S4. (a1–d1) Fluorescence responses of RhB in different solutions (ddH₂O, pH 7.4, pH 5.5, and pH 4.5 buffer) and concentrations in the 0.0–20.0 µg/mL range: (a2–d2) calibration curves of RhB. Figure S5. Release curves of SA-Gd₂O₃@MSN-RhB and NH₂-Gd₂O₃@MSN-RhB at different pH levels. Figure S6: Colloidal stability of SA-Gd₂O₃@MSN. Figure S7. Colloidal stability of SA-Gd₂O₃@MSN at different pH levels. Figure S8: Release of Gd³⁺ in different buffers. Figure S9: Cytotoxicity against 4T1 (a) and MCF-7 (b) cells after incubation with different concentrations of various NPs for 24 h. Figure S10: Morphology of human red blood cells. Figure S11: FCM images, mean fluorescence intensity levels, and MRI intensity levels of 4T1 cells after incubation with SA-Gd₂O₃@MSN-RhB at different times. Figure S12: H&E staining of 4T1 xenografts in Balb/c mice.

Author Contributions: Conceptualization and methodology, L.H. and Z.L.; validation, Z.L., J.G., G.Q. and M.Z.; investigation, Z.L. and G.Q.; writing—original draft preparation, Z.L., L.H. and J.G. All authors have read and agreed to the published version of the manuscript.

Funding: This research was funded by the basic scientific research business expenses of Heilongjiang Provincial Department of Education, grant number 2019-KYYWF-1251.

Institutional Review Board Statement: The animal study protocol was approved by the Animal Ethics Committee of Qiqihar Medical University (No. QMU-AECC-2021-100).

Data Availability Statement: The data presented in this study are available on request from the corresponding author.

Acknowledgments: We would like to thank the Qiqihar Medical Center Animal Center for helping with the model rats and the department of MRI at the First Affiliated Hospital of Qiqihar.

Conflicts of Interest: The author declare no conflict of interest.

References

1. Mu, W.; Chu, Q.; Liu, Y.; Zhang, N. A review on nano-based drug delivery system for cancer chemoimmunotherapy. *Nanomicro Lett.* **2020**, *12*, 142. [[CrossRef](#)] [[PubMed](#)]
2. Alsehli, M. Polymeric nanocarriers as stimuli-responsive systems for targeted tumor (cancer) therapy: Recent advances in drug delivery. *Saudi Pharm. J.* **2020**, *28*, 255–265. [[CrossRef](#)] [[PubMed](#)]
3. Dias, A.P.; da Silva Santos, S.; da Silva, J.V.; Parise-Filho, R.; Ferreira, E.L.; El Seoud, O.; Giarolla, J. Dendrimers in the context of nanomedicine. *Int. J. Pharm.* **2020**, *573*, 118814. [[CrossRef](#)] [[PubMed](#)]
4. Sajjadi, M.; Nasrollahzadeh, M.; Jaleh, B.; Soufi, G.J.; Iravani, S. Carbon-based nanomaterials for targeted cancer nanotherapy: Recent trends and future prospects. *J. Drug Target* **2021**, *29*, 716–741. [[CrossRef](#)] [[PubMed](#)]
5. Liu, G.; Zhao, X.; Zhang, Y.; Xu, J.; Xu, J.; Li, Y.; Min, H.; Shi, J.; Zhao, Y.; Wei, J.; et al. Engineering biomimetic plateosomes for pH-responsive drug delivery and enhanced antitumor activity. *Adv. Mater.* **2019**, *31*, e1900795. [[CrossRef](#)] [[PubMed](#)]
6. Correa, S.; Boehnke, N.; Deiss-Yehiely, E.; Hammond, P.T. Solution conditions tune and optimize loading of therapeutic polyelectrolytes into layer-by-layer functionalized liposomes. *ACS Nano* **2019**, *13*, 5623–5634. [[CrossRef](#)]
7. Farjadian, F.; Rooiantan, A.; Mohammadi-Samani, S.; Hosseini, M. Mesoporous silica nanoparticles: Synthesis, pharmaceutical applications, biodistribution, and biosafety assessment. *Chem. Eng. J.* **2019**, *359*, 684–705. [[CrossRef](#)]
8. Gisbert-Garzarán, M.; Manzano, M.; Allet-Regí, M.V. Mesoporous Silica Nanoparticles for the treatment of complex bone diseases: Bone cancer, bone infection and osteoporosis. *Pharmaceutics*. **2020**, *12*, 83. [[CrossRef](#)]
9. Ow, H.; Larson, D.R.; Srivastava, M.; Baird, B.A.; Webb, W.W.; Wiesner, U. Bright and stable core-shell fluorescent silica nanoparticles. *Nano Lett.* **2005**, *5*, 113–117. [[CrossRef](#)]
10. Benezra, M.; Penate-Medina, O.; Zanzonico, P.B.; Schaer, D.; Ow, H.; Burns, A.; DeStanchina, E.; Longo, V.; Herz, E.; Iyer, S.; et al. Multimodal silica nanoparticles are effective cancer-targeted probes in a model of human melanoma. *J. Clin. Investig.* **2011**, *21*, 2768–2780. [[CrossRef](#)]
11. Aziz, M.U.; Singh, S. Computed tomography of coronary artery atherosclerosis: A review. *J. Med. Imaging Radiat. Sci.* **2021**, *52*, 19–39. [[CrossRef](#)] [[PubMed](#)]
12. Asch, D.; DeWitt, G.; Hooley, R. Incidental Breast Findings on Computed Tomography and MR Imaging. *Radiol. Clin. North Am.* **2021**, *59*, 551–567. [[CrossRef](#)] [[PubMed](#)]

13. Petranović Ovčariček, P.; Giovanella, L.; Carrió Gasset, I.; Hindié, E.; Huellner, M.W.; Luster, M.; Piccardo, A.; Weber, T.; Talbot, J.N.; Verburg, F.A. The EANM practice guidelines for parathyroid imaging. *Eur. J. Nucl. Med. Mol. Imaging*. **2021**, *48*, 2801–2822. [[CrossRef](#)]
14. van Dyk, S.; Khaw, P.; Lin, M.Y.; Chang, D.; Bernshaw, D. Ultrasound-guided brachytherapy for cervix cancer. *Clin. Oncol.* **2021**, *33*, 403–411. [[CrossRef](#)] [[PubMed](#)]
15. Smits, M. MRI biomarkers in neuro-oncology. *Nat. Rev. Neurol.* **2021**, *17*, 486–500. [[CrossRef](#)] [[PubMed](#)]
16. Jamgotchian, L.; Vaillant, S.; Selingue, E.; Doerflinger, A.; Belime, A.; Vandamme, M.; Pinna, G.; Ling, W.L.; Gravel, E.; Mériaux, S.; et al. Tumor-targeted superfluorinated micellar probe for sensitive *in vivo* ¹⁹F-MRI. *Nanoscale*. **2021**, *13*, 2373–2377. [[CrossRef](#)] [[PubMed](#)]
17. Li, C.; Lu, D.; Wang, H.; Allen, A.; Fang, P. Enhanced Photocatalytic Activity of Directly Assembled Fe₂O₃/Gd₂O₃@TiO₂-Based Nanosheets. *J. Nanosci. Nanotechnol.* **2019**, *19*, 2678–2687. [[CrossRef](#)]
18. Wu, T.; Su, J.; Li, Y.; Zhao, H.; Zhang, Y.; Zhang, M.; Wu, B. Wear Resistance Mechanism of Alumina Ceramics Containing Gd₂O₃. *Materials* **2018**, *11*, 2054. [[CrossRef](#)]
19. Tambe, P.; Kumar, P.; Paknikar, K.M.; Gajbhiye, V. Decapeptide functionalized targeted mesoporous silica nanoparticles with doxorubicin exhibit enhanced apoptotic effect in breast and prostate cancer cells. *Int. J. Nanomed.* **2018**, *13*, 7669–7680. [[CrossRef](#)]
20. Slapak, E.J.; Kong, L.; El Mandili, M.; Nieuwland, R.; Kros, A.; Bijlsma, M.F.; Spek, C.A. ADAM9-Responsive Mesoporous Silica Nanoparticles for Targeted Drug Delivery in Pancreatic Cancer. *Cancers* **2021**, *13*, 3321. [[CrossRef](#)]
21. Wu, Z.Y.; Lee, C.C.; Lin, H.M. Hyaluronidase-Responsive Mesoporous Silica Nanoparticles with Dual-Imaging and Dual-Target Function. *Cancers* **2019**, *11*, 697. [[CrossRef](#)] [[PubMed](#)]
22. Zhuang, J.; Chen, S.; Hu, Y.; Yang, F.; Huo, Q.; Xie, N. Tumour-Targeted and Redox-Responsive Mesoporous Silica Nanoparticles for Controlled Release of Doxorubicin and an siRNA Against Metastatic Breast Cancer. *Int. J. Nanomed.* **2021**, *16*, 1961–1976. [[CrossRef](#)] [[PubMed](#)]
23. Akram, Z.; Aati, S.; Ngo, H.; Fawzy, A. pH-dependent delivery of chlorhexidine from PGA grafted mesoporous silica nanoparticles at resin-dentin interface. *J. Nanobiotechnology* **2021**, *19*, 19–43. [[CrossRef](#)] [[PubMed](#)]
24. Mladenović, M.; Morgan, I.; Ilić, N.; Saoud, M.; Pergal, M.V.; Kaluđerović, G.N.; Knežević, N.Ž. pH-Responsive Release of Ruthenium Metallotherapeutics from Mesoporous Silica-Based Nanocarriers. *Pharmaceutics* **2021**, *13*, 460. [[CrossRef](#)]
25. Bernardos, A.; Božik, M.; Montero, A.; Pérez-Esteve, É.; García-Casado, E.; Lhotka, M.; Fraňková, A.; Marcos, M.D.; Barat, J.M.; Martínez-Mañez, R.; et al. Secreted Enzyme-Responsive System for Controlled Antifungal Agent Release. *Nanomaterials* **2021**, *11*, 1280. [[CrossRef](#)] [[PubMed](#)]
26. Xu, Y.; Xiao, L.; Chang, Y.; Cao, Y.; Chen, C.; Wang, D. pH and Redox Dual-Responsive MSN-S-S-CS as a Drug Delivery System in Cancer Therapy. *Materials* **2020**, *13*, 1279. [[CrossRef](#)]
27. Li, X.; Zhang, X.; Zhao, Y.; Sun, L. Fabrication of biodegradable Mn-doped mesoporous silica nanoparticles for pH/redox dual response drug delivery. *J. Inorg. Biochem.* **2020**, *202*, 110887. [[CrossRef](#)]
28. Salinas, Y.; Brüggemann, O.; Monkowius, U.; Teasdale, I. Visible Light Photocleavable Ruthenium-Based Molecular Gates to Reversibly Control Release from Mesoporous Silica Nanoparticles. *Nanomaterials* **2020**, *10*, 1030. [[CrossRef](#)]
29. Li, X.; Wang, Z.; Xia, H. Ultrasound Reversible Response Nanocarrier Based on Sodium Alginate Modified Mesoporous Silica Nanoparticles. *Front Chem.* **2019**, *7*, 59. [[CrossRef](#)]
30. Pandele, A.M.; Andronescu, C.; Ghebaur, A.; Garea, S.A.; Iovu, H. New Biocompatible Mesoporous Silica/Polysaccharide Hybrid Materials as Possible Drug Delivery Systems. *Materials* **2018**, *12*, 15. [[CrossRef](#)]
31. Jiao, J.; Li, X.; Zhang, S.; Liu, J.; Di, D.; Zhang, Y.; Zhao, Q.; Wang, S. Redox and pH dual-responsive PEG and chitosan-conjugated hollow mesoporous silica for controlled drug release. *Mater. Sci. Eng. C* **2016**, *67*, 26–33. [[CrossRef](#)] [[PubMed](#)]
32. Sanchez-Ballester, N.M.; Bataille, B.; Soulaïrol, I. Sodium alginate and alginic acid as pharmaceutical excipients for tablet formulation: Structure-function relationship. *Carbohydr. Polym.* **2021**, *270*, 118399. [[CrossRef](#)] [[PubMed](#)]
33. Tavassoli, K.E.; Shekarchizadeh, H.; Masoudpour, B.M. Development of edible films and coatings from alginates and carrageenans. *Carbohydr. Polym.* **2016**, *137*, 360–374. [[CrossRef](#)] [[PubMed](#)]
34. Mori, M.; Asahi, R.; Yamamoto, Y.; Mashiko, T.; Yoshizumi, K.; Saito, N.; Shirado, T.; Wu, Y.; Yoshimura, K. Sodium Alginate as a Potential Therapeutic Filler: An In Vivo Study in Rats. *Mar. Drugs*. **2020**, *18*, 520. [[CrossRef](#)] [[PubMed](#)]
35. Dwivedi, L.M.; Baranwal, K.; Gupta, S.; Mishra, M.; Sundaram, S.; Singh, V. Antibacterial nanostructures derived from oxidized sodium alginate-ZnO. *Int. J. Biol. Macromol.* **2020**, *149*, 1323–1330. [[CrossRef](#)] [[PubMed](#)]
36. Alshhab, A.; Yilmaz, E. Sodium alginate/poly(4-vinylpyridine) polyelectrolyte multilayer films: Preparation, characterization and ciprofloxacin HCl release. *Int. J. Biol. Macromol.* **2020**, *147*, 809–820. [[CrossRef](#)] [[PubMed](#)]
37. Hou, X.; Xue, Z.; Xia, Y.; Qin, Y.; Zhang, G.; Liu, H.; Li, K. Effect of SiO₂ nanoparticle on the physical and chemical properties of eco-friendly agar/sodium alginate nanocomposite film. *Int. J. Biol. Macromol.* **2019**, *125*, 1289–1298. [[CrossRef](#)]
38. Yang, H.; Chen, Y.; Chen, Z.; Geng, Y.; Xie, X.; Shen, X.; Li, T.; Li, S.; Wu, C.; Liu, Y. Chemo-photodynamic combined gene therapy and dual-modal cancer imaging achieved by pH-responsive alginate/chitosan multilayer-modified magnetic mesoporous silica nanocomposites. *Biomater. Sci.* **2017**, *5*, 1001–1013. [[CrossRef](#)]
39. Zhang, Y.W.; Tu, L.L.; Tang, Z.; Wang, Q.; Zheng, G.L.; Yin, L.N. pH-sensitive chitosan-deoxycholic acid/alginate nanoparticles for oral insulin delivery. *Pharm. Dev. Technol.* **2021**, *26*, 943–952. [[CrossRef](#)]

40. Zhao, L.; Yin, S.; Ma, Z. Ca^{2+} -triggered pH-response sodium alginate hydrogel precipitation for amplified sandwich-type impedimetric immunosensor of tumor marker. *ACS Sens.* **2019**, *4*, 450–455. [[CrossRef](#)]
41. Klyachko, N.L.; Manickam, D.S.; Brynskikh, A.M.; Uglanova, S.V.; Li, S.; Higginbotham, S.M.; Bronich, T.K.; Batrakova, E.V.; Kabanov, A.V. Cross-linked antioxidant nanozymes for improved delivery to CNS. *Nanomedicine* **2012**, *8*, 119–129. [[CrossRef](#)] [[PubMed](#)]
42. Pandey, S.; Ramontja, J. Sodium alginate stabilized silver nanoparticles-silica nanohybrid and their antibacterial characteristics. *Int. J. Biol. Macromol.* **2016**, *93*, 712–723. [[CrossRef](#)] [[PubMed](#)]
43. Zhao, Q.; Han, B.; Wang, Z.; Gao, C.; Peng, C.; Shen, J. Hollow chitosan-alginate multilayer microcapsules as drug delivery vehicle: Doxorubicin loading and in vitro and in vivo studies. *Nanomedicine* **2007**, *3*, 63–74. [[CrossRef](#)]
44. Zhao, Q.; Jia, L.; Zhu, W.; Sun, C.; Di, D.; Ying, Z.; Wang, P.; Wang, Z.; Wang, S. Dual-stimuli responsive hyaluronic acid-conjugated mesoporous silica for targeted delivery to CD44-overexpressing cancer cells. *Acta Biomater.* **2015**, *23*, 147–156. [[CrossRef](#)] [[PubMed](#)]
45. Guo, X.; Wu, Z.; Li, W.; Wang, Z.; Li, Q.; Kong, F.; Zhang, H.; Zhu, X.; Du, Y.P.; Jin, Y.; et al. Appropriate Size of Magnetic Nanoparticles for Various Bioapplications in Cancer Diagnostics and Therapy. *ACS Appl. Mater. Interfaces* **2016**, *8*, 3092–3106. [[CrossRef](#)]
46. He, K.; Li, J.; Shen, Y.; Yu, Y. pH-Responsive polyelectrolyte coated gadolinium oxide-doped mesoporous silica nanoparticles ($\text{Gd}_2\text{O}_3@$ MSNs) for synergistic drug delivery and magnetic resonance imaging enhancement. *J. Mater. Chem. B* **2019**, *7*, 6840–6854. [[CrossRef](#)] [[PubMed](#)]
47. Qi, Q.; Chi, W.; Li, Y.; Qiao, Q.; Chen, J.; Miao, L.; Zhang, Y.; Li, J.; Ji, W.; Xu, T.; et al. A H-bond strategy to develop acid-resistant photoswitchable rhodamine spirolactams for super-resolution single-molecule localization microscopy. *Chem. Sci.* **2019**, *10*, 4914–4922. [[CrossRef](#)]
48. Zhao, J.; Yang, H.; Li, J.; Wang, Y.; Wang, X. Fabrication of pH-responsive PLGA(UCNPs/DOX) nanocapsules with upconversion luminescence for drug delivery. *Sci. Rep.* **2017**, *7*, 18014. [[CrossRef](#)]
49. Feng, W.; Nie, W.; He, C.; Zhou, X.; Chen, L.; Qiu, K.; Wang, W.; Yin, Z. Effect of pH-responsive alginate/chitosan multilayers coating on delivery efficiency, cellular uptake and biodistribution of mesoporous silica nanoparticles based nanocarriers. *ACS Appl. Mater. Interfaces* **2014**, *6*, 8447–8460. [[CrossRef](#)]
50. Di, M.A.; Kucharczyk, P.; Capakova, Z.; Humpolicek, P.; Sedlarik, V. Enhancement of temozolomide stability by loading in chitosan-carboxylated polylactide-based nanoparticles. *J. Nanopart. Res.* **2017**, *19*, 71.
51. Chen, H.; Wang, Y.; Wang, Q.; Li, J.; Yang, S.; Zhu, Z. Bifunctional organic polymeric catalysts with a tunable acid-base distance and framework flexibility. *Sci. Rep.* **2014**, *4*, 6475. [[CrossRef](#)] [[PubMed](#)]
52. Thai, H.; Thuy, N.C.; Thi, T.L.; Thi, T.M.; Duc, M.H.; Thi, T.N.T.; Duc, L.G.; Van, C.M.; Dai, T.L.; Long, B.G.; et al. Characterization of chitosan/alginate/lovastatin nanoparticles and investigation of their toxic effects in vitro and in vivo. *Sci. Rep.* **2020**, *10*, 909. [[CrossRef](#)] [[PubMed](#)]
53. Xu, W.; Lu, Y. A smart magnetic resonance imaging contrast agent responsive to adenosine based on a DNA aptamer-conjugated gadolinium complex. *Chem. Commun.* **2011**, *47*, 4998–5000. [[CrossRef](#)]
54. Jiang, W.; Fang, H.; Liu, F.; Zhou, X.; Zhao, H.; He, X.; Guo, D. PEG-coated and Gd-loaded fluorescent silica nanoparticles for targeted prostate cancer magnetic resonance imaging and fluorescence imaging. *Int. J. Nanomed.* **2019**, *14*, 5611–5622. [[CrossRef](#)] [[PubMed](#)]
55. Huang, Y.; Ding, X.; Qi, Y.; Yu, B.; Xu, F.J. Reduction-responsive multifunctional hyperbranched polyaminoglycosides with excellent antibacterial activity, biocompatibility and gene transfection capability. *Biomaterials* **2016**, *106*, 134–143. [[CrossRef](#)] [[PubMed](#)]
56. Yan, T.; Kong, S.; Ouyang, Q.; Li, C.; Hou, T.; Chen, Y.; Li, S. Chitosan-Gentamicin Conjugate Hydrogel Promoting Skin Scald Repair. *Mar. Drugs.* **2020**, *18*, 233. [[CrossRef](#)]
57. Li, Z.; Guo, J.; Zhang, M.; Li, G.; Hao, L. Gadolinium-Coated Mesoporous Silica Nanoparticle for Magnetic Resonance Imaging. *Front Chem.* **2022**, *10*, 837032. [[CrossRef](#)] [[PubMed](#)]
58. Lv, Y.; Li, J.; Chen, H.; Bai, Y.; Zhang, L. Glycyrrhetic acid-functionalized mesoporous silica nanoparticles as hepatocellular carcinoma-targeted drug carrier. *Int. J. Nanomed.* **2017**, *12*, 4361–4370. [[CrossRef](#)]
59. Chen, Y.; Chen, H.; Zeng, D.; Tian, Y.; Chen, F.; Feng, J.; Shi, J. Core/shell structured hollow mesoporous nanocapsules: A potential platform for simultaneous cell imaging and anticancer drug delivery. *ACS Nano* **2010**, *4*, 6001–6013. [[CrossRef](#)]
60. Zhang, X.; Wang, Y.; Zhao, Y.; Sun, L. pH-responsive drug release and real-time fluorescence detection of porous silica nanoparticles. *Mater. Sci. Eng. C Mater. Biol. Appl.* **2017**, *77*, 19–26. [[CrossRef](#)]